Journal of Materials Chemistry A

Catalytic Mechanism and Design Principle of Coordinately Unsaturated Single Metal Atom-Doped Covalent Triazine Frameworks with High Activity and Selectivity for CO2 Electroreduction

Journal:	*Journal of Materials Chemistry A*
Manuscript ID	TA-ART-11-2020-010875.R1
Article Type:	Paper
Date Submitted by the Author:	11-Dec-2020

Complete List of Authors:	Gong, Lele; Beijing University of Chemical Technology Wang, Xiaowei; University of North Texas Zheng, Tao; Northwestern Polytechnical University Liu, Jerry; University of North Texas Wang, Jie; University of North Texas Yang, Yu-Chia; University of North Texas Zhang, Jing; Northwestern Polytechnical University, State Key Laboratory of Solidification Processing Han, Xiao; Northwestern Polytechnical University, School of materials science and engineering Zhang, Lipeng; Beijing University of Chemical Technology, Xia, Zhenhai; University of North Texas, Department of Materials Science and Engineering

Catalytic Mechanism and Design Principle of Coordinately Unsaturated Single Metal Atom-Doped Covalent Triazine Frameworks with High Activity and Selectivity for CO_2 Electroreduction

Lele Gong[1], Xiaowei Wang[2], Tao Zheng[3], Jerry Liu[2], Jie Wang[2], Yu-Chia Yang[2], Jing Zhang[3], Xiao Han[3], Lipeng Zhang[1], Zhenhai Xia[2*]*

[1] College of Chemical Engineering, Beijing University of Chemical Technology, Beijing, 100029, China

[2] Department of Materials Science and Engineering, University of North Texas, Denton, TX 76203, USA

[3]School of Materials Science and Engineering, Northwestern Polytechnical University, Xi'an, 710072, China

* Corresponding authors: zhanglipeng2011@gmail.com, Zhenhai.xia@unt.edu

Abstract

Electrochemical conversion of carbon dioxide (CO_2) to chemicals or fuels can promote effectively carbon capture and utilization, and reduce greenhouse gas emission but a serious impediment to the process is to find highly active electrocatalysts that can selectively produce desired products. Herein, we have established the design principles based on the density functional theory calculations to screen the most promising catalysts from the family of coordinately-unsaturated/saturated transition metal (TM) embedded into covalent organic frameworks (TM-COFs). An intrinsic descriptor has been discovered to correlate the molecular structures of the active centers with both the activity and selectivity of the catalysts. Among all the catalysts, coordinately-unsaturated Ni-doped covalent triazine framework (Ni-CTF) is identified as one of the best electrocatalysts with the lowest overpotential (0.34 V) for CO_2 reduction toward CO while inhibiting side products, H_2 and formic. Compared with coordinately-

saturated TM-COFs and noble metals (e.g. Au and Au), TM-CTFs exhibit higher catalytic activity and stronger inhabitation to the side products. The predictions are supported by previous experimental results. This study provides an effective strategy and predictive tool for developing desired catalysts with high activity and selectivity.

1 Introduction

Electrocatalytic carbon dioxide (CO_2) reduction is a promising strategy to reduce CO_2 in the atmosphere and produce carbon neutral fuels or industrial chemicals, which would alleviate the global greenhouse issues and enable sustainable development in energy economy and chemical industry.[1-5] In CO_2 reduction reaction (CO_2RR), carbon monoxide (CO) is one of the primary products when using catalysts such as iron, cobalt, nickel-based materials.[6] In particular, their single-atom catalysts (SACs) become popular in CO_2 conversion.[7-11] Due to the high chemical inertness of CO_2 molecules, however, there is a large energy barrier in the elementary reaction of $*CO_2$ chemisorption or CO desorption according to the first-principles calculation.[12-13] This will undoubtedly hinder the reaction-rate and increase the overpotential for electrocatalytic reduction of CO_2 to CO. Moreover, the undesirable side-reaction of hydrogen evolution reaction (HER) will also share the catalysts in aqueous electrolytes because of its similar equilibrium potentials to CO_2RR.[14] Therefore, there is still an urgent desire to solve the problems of low efficiency and poor selectivity in CO_2RR, as well as sluggish reaction kinetics. For this purpose, the development of highly effective electrocatalysts for CO_2RR is becoming increasingly important.

Previous work has shown that the catalyst structures with coordinately unsaturated metal moieties seem to be more active in improving the CO_2RR catalytic performance.[15-16] For example, it has been demonstrated that bulk Pt or Cu with fewer coordination numbers will enhance *CO bonding strength, and thus optimize their CO_2RR catalytic performance.[17-18] Bao *et al.* studied the CO_2RR catalytic performance on coordinately unsaturated Ni-N_x active sites anchored within porous carbon and

concluded that the catalysts with unsaturated Ni-N_x sites exhibited high current density and Faradaic efficiency of CO_2RR toward CO.[19]

Covalent triazine frameworks (CTFs) are type of covalent organic frameworks (COFs) with porous structure, high BET surface, and can be flexibly designed in different geometric shape, sizes and reactive groups.[20] Unlike most COFs that are incorporated with coordinately-saturated transition metals (TMs)[21-25], the inborn defects in CTF frameworks allow TMs to be embedded to form coordinately-unsaturated active sites, and provide a relaxed steric hindrance in their catalytic unit for changeable adsorption modes of reactants, both of which are considered as effective strategies to improve their catalytic performance.[26-28] Nakanishi *et al.* investigated CTFs modified with coordinately-unsaturated TM for ORR (oxygen reduction reaction), HER and CO_2RR, and found that the TM-doped CTFs had higher catalytic activity than coordinately-saturated TM-doped TPP (tetraphenylporphyrin) under the same conditions.[29-33] They attributed this activity improvement to the unsaturated TM on CTFs, which had more flexible adsorption modes for breaking the scaling relation in adsorption energies of the intermediates. However, the underlying catalytic mechanism of the unsaturated TM is still controversial so far. Furthermore, there lacks design principles to guide the synthesis of the TM-CTFs. In particular, there is no effective approach to predict quantitatively the selectivity of catalysts for CO_2RR due to its complexity of the intermediates and complete reactions.

In this paper, we systematically explored the catalytic performance of various TM-doped CTFs for CO_2RR toward CO by using DFT methods. The stabilities, electronic structures, reaction pathways and overpotentials were calculated to predict the catalytic activity and selectivity of those TM-CTFs for CO_2 electroreduction. The calculations were supported by previous the experimental results. This work thus provides a theoretical base for understanding of underlying catalytic mechanism and an effective approach for screening of TM-COFs for CO_2RR.

2 Results and discussion

2.1 Structures and stability of TM-CTFs

We have designed a series of TM-doped CTFs, including all 3d, 4d, 5d TM except Tc, Cd, Hg and lanthanides (La-Lu) due to their toxic/radioactive property. As shown in Figure 1A, a TM is bonded with three surrounding nitrogen atoms to form a TM-N_3 catalytic unit. The average values of bond lengths for Ni-N and Co-N in their catalyst forms were calculated to be 2.11 Å and 2.08 Å (Table S9), which are very close to the experimental results (2.08 ± 0.05 and 2.00 ± 0.10) for Ni-CTF and Co-CTF[26], respectively, indicating that these structures are reasonable.

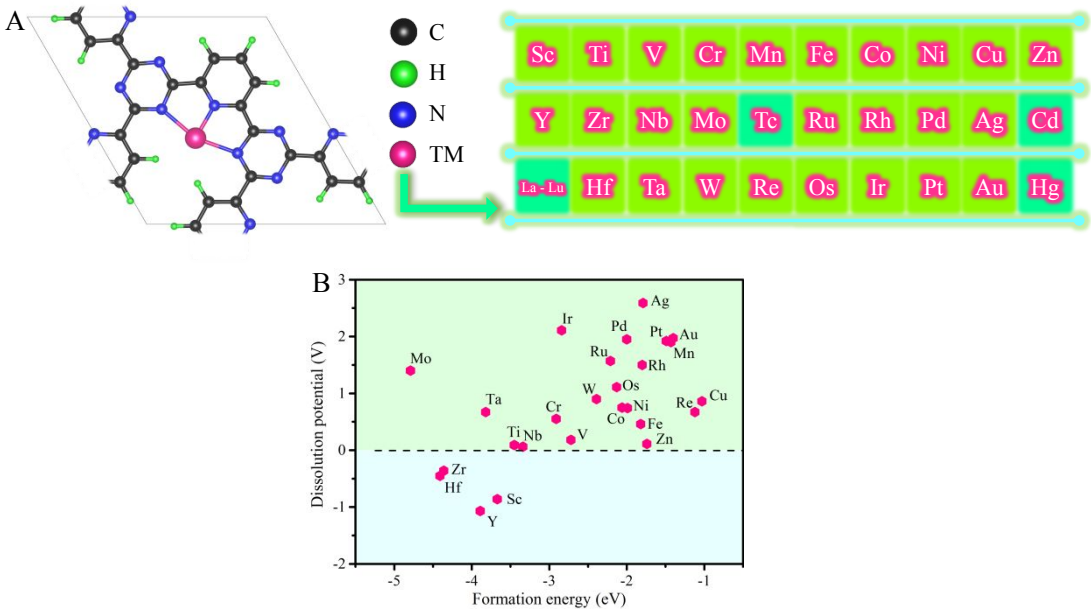

Figure 1. (A) Molecular structure of TM-doped CTFs, the black, green, blue and pink balls represent carbon, hydrogen, nitrogen, and TM atoms; (B) calculated formation energy and dissolution potential of all TM-CTFs.

We have explored the thermodynamical and electrochemical stabilities of TM-CTFs by calculating the formation energy (E_f) and dissolution potential (U_{diss}), respectively (Support Information).[34] A stable electrocatalyst should have negative formation energy ($E_f < 0$) and positive dissolution potential ($U_{diss} > 0$), making it easy to synthesize (thermodynamically stable) and difficult to dissolve in aqueous solution (electrochemically stable).[35] As shown in Figure 1B, the formation energy values (x axis) of all the TM-CTFs considered in this study are well below zero, indicating that all the TM-CTFs are thermodynamically stable, but some of them (e.g., Sc-, Y-, Zr-,

Hf-CTFs) are electrochemically unstable in term of the dissolution potential (y axis). Thus, most of these designed catalysts are thermodynamically and electrochemically stable; those unstable TM-CTFs will be excluded in the following analysis. Actually, some TM-CTFs have been successfully synthesized for electrocatalytic applications.[36-44]

2.2 Electronic structures and CO_2RR catalytic pathways of TM-CTFs

2.2.1. CO_2 adsorption

In electrochemical reactions, the first elementary reaction is usually involved in the adsorption of gaseous reactants on catalyst surface, which is a critical step to determine catalytic mechanism (e.g., associate or dissociate adsorption modes).[45-46] Thus, we simulated CO_2RR on various TM-CTFs, starting from CO_2 adsorption. As shown in Figure 2A and 2B, there are four possible CO_2 chemisorption configurations on TM-CTFs, i.e., end-on (*CO_2-1 and *CO_2-2) and side-on (*CO_2-3 and *CO_2-4) modes. Our calculations revealed that most of the TM-CTFs (TM = 3d/Ti, V, Cr, Fe, Co, Ni; 4d/Nb, Mo, Ru, Rh; 5d/Ta, W, Re, Os, Ir) can directly capture CO_2 molecules with negative adsorption energy ($\Delta G_{*CO2} < 0$ eV), indicating that the adsorption is spontaneous. CO_2 molecules can be readily adsorbed on these catalysts in mode *CO_2-3 (Figure 2B), in which both the C and O atoms in CO_2 were co-adsorbed simultaneously. In contrast, the TM-CTFs with d^9 or d^{10} electrons, including Cu, Zn, Pd, Ag, Pt, Au, require an additional electron to promote CO_2 chemisorption. Since CO_2 chemisorption occurs after the TM acquires an electron to change its valence state, CO_2 molecules are preferentially adsorbed in mode *CO_2-3 on Cu- and Pd-CTFs, but in mode *CO_2-1 on Zn-, Ag-, Pt- and Au-CTFs. All these six catalysts also have negative adsorption energy ($\Delta G_{*CO2} < 0$ eV) for CO_2 chemisorption except Cu-CTF with a negligible positive adsorption energy ($\Delta G_{*CO2} = 0.08$ eV). Therefore, CO_2 adsorption in the first elementary reaction is spontaneous on all TM-CTFs in mode 1 or 3.

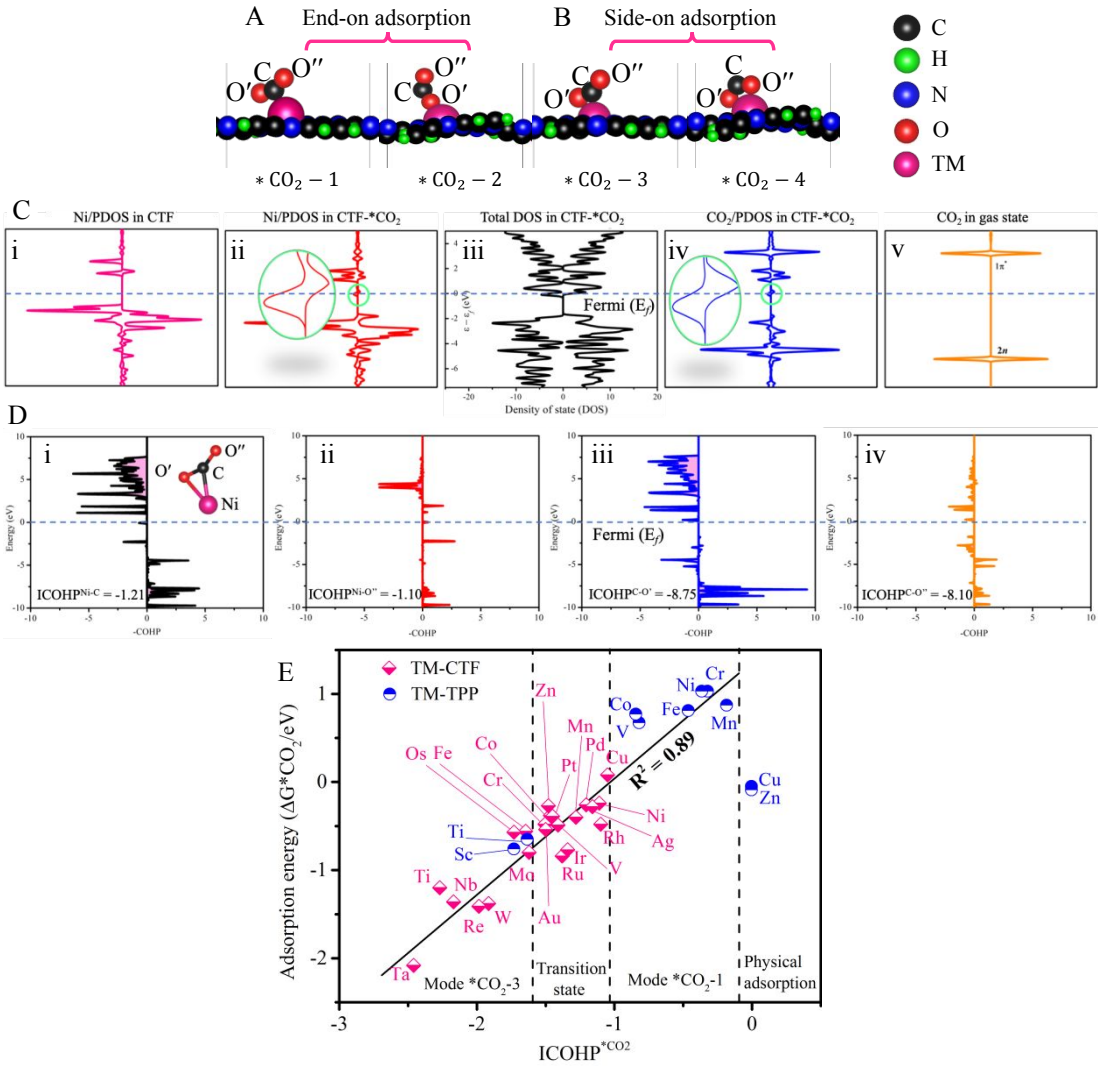

Figure 2. Four possible *CO_2 chemisorption configurations on TM-CTFs, classified into (A) end-on and (B) side-on models. (C) The DOS and PDOS of Ni-CTFs before and after adsorbing CO_2 including i) Ni/PDOS in Ni-CTF, ii) Ni/PDOS in Ni-CTF-*CO_2 (adsorbing CO_2), iii) TDOS in Ni-CTF-*CO_2, iv) *CO_2 adsorbate/PDOS in Ni-CTF-*CO_2, v) CO_2/PDOS in CO_2 free molecules; (D) The COHP and corresponding ICOHP values of Ni-CTF, from left to right including i) Ni-C, ii) Ni-O′, iii) C-O′, and iv) C-O″, respectively. The inset configuration of Ni-CTF-*CO_2 was simplified for clarity. (E) CO_2 adsorption energy ΔG_{*CO2} as a function of $ICOHP^{*CO2}$ for TM-CTF and TM-TPP[49].

To understand the diversities of CO_2 chemisorption modes and adsorption mechanism, we analyzed the density of state (DOS) and partial density of state (PDOS)

of those TM-CTFs before and after adsorbing CO_2. As shown in Figure 2C, two new hybridized energy levels were found near the Fermi level, namely *d*-π* (occ) and *d*-π* (unocc) formed by the interaction between 1π* anti-bonding orbitals of CO_2 and *d* orbit of TM-CTFs, resulting in partially occupied 1π* orbitals below the Fermi level. This interaction will help strengthen CO_2 adsorption and reduce the total energy of overall system. Thus, the location and overlapping area of *d*-π* (occ) have a significant effect on CO_2 adsorption capacity. Figure S4 shows the information about the *d*-π* (occ) and *d*-π* (unocc) of 3*d* TM-CTFs. The *d*-π* (occ) of Ti-CTF have a large overlapping area and located far from the Fermi level, which implied a strong interaction with the adsorbed CO_2. In contrast, the positive adsorption energy (ΔG_{*CO2} = 0.08 eV) of CO_2 on Cu-CTF surface can mainly be explained by the small overlapping area and nearby location of *d*-π* (occ). Others have moderate overlapping area and location of *d*-π* (occ) leading to appropriate adsorption energy (Figure S4).

We further analyzed the crystal orbital Hamilton population (COHP) to gain an in-depth understanding of the *d*-π* interaction between the *CO_2 adsorbates and TM-CTFs. Figure 2C and Figure S6 show COHP of typical TM-CTFs. For the bonds of C-O′ and C-O′′ (O′ and O′′ refer to the oxygen atoms close to and far from the metal ion, respectively, as illustrated in Figure 2A) in *CO_2 adsorbates, some electrons have already occupied the anti-bonding orbital (-COHP < 0) below the Fermi level, in sharp contrast to free CO_2 gaseous molecules with all the electrons distributed in the bonding orbital (-COHP > 0) in Figure S5, indicating that these two bonds are slightly weakened. This is very important to understand the mechanism of the next hydrogenation reaction, which will be discussed later.

To quantify the *d*-π* interaction, the integrated-COHP (ICOHP) was calculated by integrating the electronic states up to the highest occupied energy level (Fermi level). Normally, there is a negative correlation between the ICOHP value and the strength of *d*-π* interaction, that is, a more negative ICOHP leads to a stronger *d*-π* coupling. As shown in Figure 2D, the ICOHP values for the bonds of Ni-C and Ni-O′ are -1.21 and -1.10, respectively. Whereas, Ti-CTF has the highest ICOHP values of Ti-C bond (-1.62) and Ti-O′ bond (-2.93) (shown in Figure S6), indicating the strongest *d*-π*

interaction among the 3*d* TM-CTFs. This could explain why Ti-CTF catalyst has the lowest CO_2 adsorption energies. To compare the difference between modes *CO_2-1 and *CO_2-3, we utilized the average ICOHP values of TM-C and TM-O bonds to represent whole *d*-π* interaction (Table S6). An approximately linear correlation (with R^2 of 0.89) between the ICOHP value ($ICOHP^{*CO2}$) and the CO_2 adsorption energies (ΔG_{*CO2}) merges, as shown in Figure 2E, revealing the important role played by *d*-π* coupling in the adsorption of CO_2 intermediate on all TM-CTFs. Interestingly, Figure 2E can be divided into several regimes, each of which corresponds to an adsorption mode. Notably, the adsorption energy of coordinately-saturated TM-TPPs[49] also follows the linear relationship with $ICOHP^{*CO2}$ but is much higher than that of TM-CTFs. Thus, the ICOHP could be used to predict the strength and modes of CO_2 chemisorption on TM-CTFs.

2.2.2. CO_2 activation and reaction pathways

We found that there were four possible reaction pathways in CO_2RR toward CO after CO_2 adsorption, as illustrated in Figure 3A. The first pathway (denoted by Path 1) is O′ protonation in CO_2 activation, followed by the dissociation of *COOH to form *OH and *CO. *OH further reacts into H_2O while *CO desorbs from TM-CTFs. This occurs on Ti, V, Cr, Nb, Ta, W, and Re-CTFs. Taking Ti-CTF as an example, the free energy change of O′ protonation is -0.68 eV, which is much lower than that of O″ (0.13 eV). As a proton attacks O′ atom, the weakened bond of C-O′ in mode *CO_2-3 was broken into two independent intermediates of *OH and *CO, which are adsorbed on the same TM ion, as shown in Figure 3A (Path 1). In Paths 2 and 3, which occurs on Mn, Fe, Co, Ni, Cu, Mo, Ru, Rh, Pd, Os, and Ir-based TM-CTFs, both O′ and O″ can be attacked by protons in the hydronation reaction because the reaction energy to attack O′ atom is almost the same as attacking O″ atom. For example, for Ni-CTF the energy difference for attacking O′ and O″ is 0.07eV. When O′ or O″ is protonated, TM-O′ will break to form *COOH with only carbon atom bonded to TM, as shown in Figure 3A. For the TM-CTFs with mode *CO_2-1, Zn-CTF, for example, has identical bond length for C-O′ and C-O″ bonds, leading to the same free energy change in O

protonation, as shown in Figure 3A (Path 4). From above analysis, CO_2RR pathways toward CO are mainly determined by the first protonation besides the configuration of CO_2 chemisorption. Since the free energy change of O′ protonation is usually lower than that of O″, O′ atom is more likely to be attacked by protons in aqueous solutions.

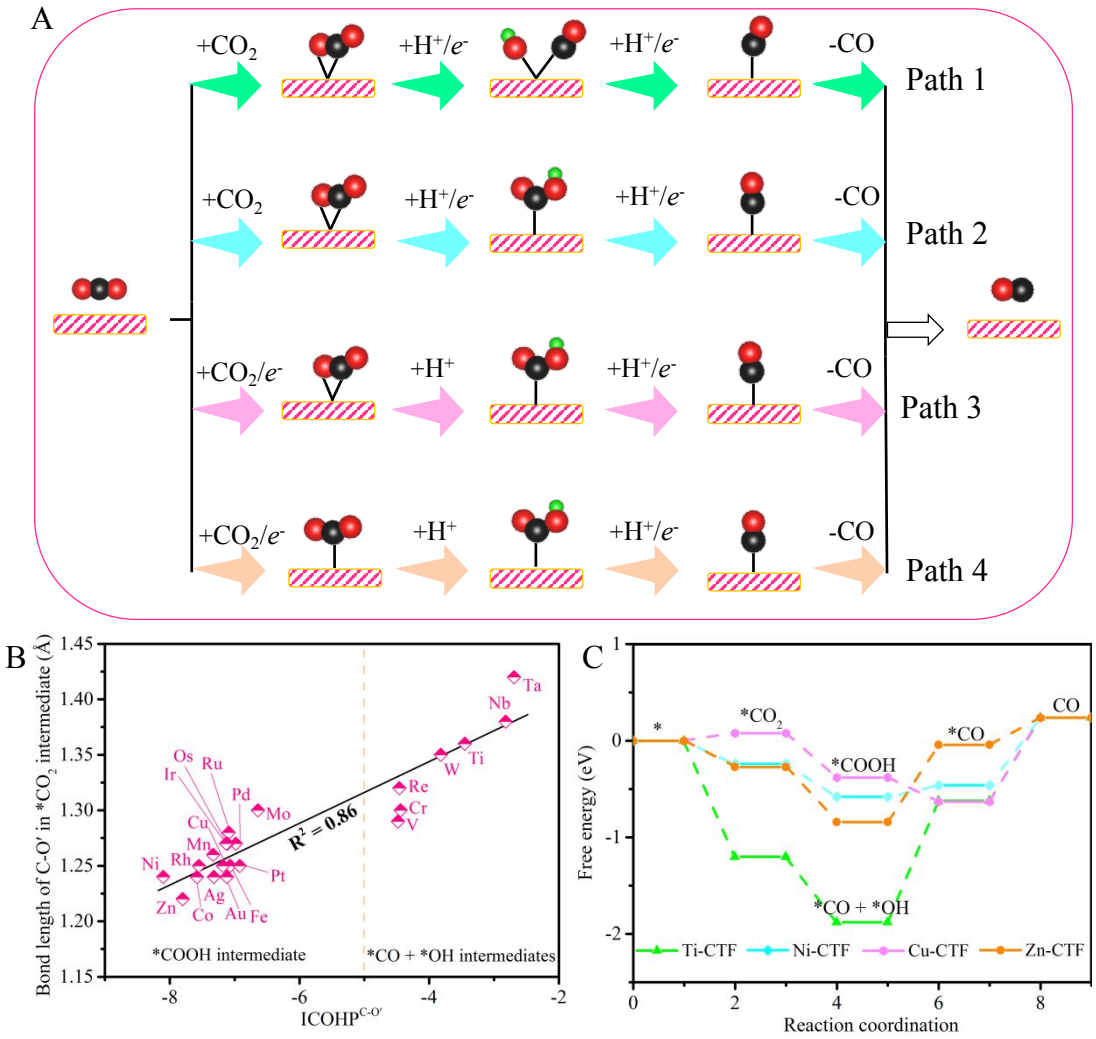

Figure 3. (A) Four CO_2RR catalytic mechanisms to form CO, (Paths 1-4). (B) The ICOHP of C-O′ in *CO_2 intermediates as a function of its correspond bond length. (C) The free energy diagrams of representative catalysts: including Ti-CTF, Ni-CTF, Cu-CTF, and Zn-CTF.

We found that there were four possible reaction pathways in CO_2RR toward CO after CO_2 adsorption, as illustrated in Figure 3A. The first pathway (denoted by Path 1)

is O′ protonation in CO_2 activation, followed by the dissociation of *COOH to form *OH and *CO. *OH further reacts into H_2O while *CO desorbs from TM-CTFs. This occurs on Ti, V, Cr, Nb, Ta, W, and Re-CTFs. Taking Ti-CTF as an example, the free energy change of O′ protonation is -0.68 eV, which is much lower than that of O′′ (0.13 eV). As a proton attacks O′ atom, the weakened bond of C-O′ in mode *CO_2-3 was broken into two independent intermediates of *OH and *CO, which are adsorbed on the same TM ion, as shown in Figure 3A (Path 1). In Paths 2 and 3, which occurs on Mn, Fe, Co, Ni, Cu, Mo, Ru, Rh, Pd, Os, and Ir-based TM-CTFs, both O′ and O′′ can be attacked by protons in the hydronation reaction because the reaction energy to attack O′ atom is almost the same as attacking O′′ atom. For example, for Ni-CTF the energy difference for attacking O′ and O′′ is 0.07eV. When O′ or O′′ is protonated, TM-O′ will break to form *COOH with only carbon atom bonded to TM, as shown in Figure 3A. For the TM-CTFs with mode *CO_2-1, Zn-CTF, for example, has identical bond length for C-O′ and C-O′′ bonds, leading to the same free energy change in O protonation, as shown in Figure 3A (Path 4). From above analysis, CO_2RR pathways toward CO are mainly determined by the first protonation besides the configuration of CO_2 chemisorption. Since the free energy change of O′ protonation is usually lower than that of O′′, O′ atom is more likely to be attacked by protons in aqueous solutions.

To understand why O′ is the target of proton attack in CO_2 activation, we analyzed the charge density distribution of *CO_2 adsorbates. Figure S7 shows the optimized adsorption configurations and charge density distribution of CO_2 chemisorbed on TM-CTFs. It is well-known that TMs can act as an electrophile to accept electrons from adsorbates, and can also serve as a nucleophile to donate lone-pair of electrons to adsorbates. This accept-donate process results in different amounts of electrons (0.30*e* to 1.10*e*) to be transferred from the catalyst to the CO_2 adsorbates. This electron transfer can remarkably activate the double bond of C=O in CO_2, leading to a significant elongation of bond length and change of bond angle. As shown in Figure S7, upon adsorbed to Ni-CTF, the C-O bonds in CO_2 were stretched to 1.24 Å (C-O′) and 1.20 Å (C-O′′) from its gaseous state (1.16 Å). Whereas, the C-O bonds were elongated even more to 1.36 Å (C-O′) and 1.21 Å (C-O′′) in Ti-CTF-*CO_2. The lower bonding strength

corresponds to higher ICOHP (e.g., $ICOHP^{C\text{-}O'}$ = -8.10 *vs* $ICOHP^{C\text{-}O''}$ = -8.75 in Ni-CTF-*CO_2, as shown in Figure 2D and Figure S6). Thus, ICOHP could be used to determine which O atom is the potential target in the CO_2 activation. In fact, there is an approximately linear correlation (with R^2 of 0.86) between the ICOHP of C-O′ bond in CO_2 intermediates ($ICOHP^{C\text{-}O'}$) and its corresponding bond length, as shown in 3B. The TMs, located on the left region ($ICOHP^{C\text{-}O'} < -5$), are favored to form *COOH intermediates in CO_2 activation. Whereas, the dissociation and independent intermediates of *CO and *OH are preferred on the TMs in right region ($ICOHP^{C\text{-}O'} > -5$).

The free energy diagrams of the typical structures (Ti-, Ni-, Cu- and Zn-CTFs), that represent four reaction pathways, are shown in Figure 3C. The third elementary reaction, *COOH hydronation (*COOH $\rightarrow$ *CO+H_2O), is the rate-determining step (RDS) for Ti-CTF and Zn-CTF, and their reaction pathways follow Paths 1 and 4, respectively. The fourth step, *CO desorption (*CO $\rightarrow$ *+CO) in Paths 2 and 3 is the RDS for Ni-CTF and Cu-CTF, respectively. The adsorption configurations of intermediates on TM-CTFs via above four catalytic mechanisms are shown in Figure S8-S11. Note that, Mn-CTF is the only case with RDS in the third elementary step of Path 2.

2.3 Catalytic Activity and Intrinsic Descriptors

Establishing the relationship between catalytic performance and descriptors would provide a theoretical guideline and tool for screening the best catalysts from a large number of catalyst candidates. While the catalytic performance is usually measured by the overpotential (η), [47-48] a predictive descriptor is more decisive to catalyst screening. We first explore the relationship between the overpotential of CO_2RR (η^{CO}) and the adsorption energy of $\Delta G_{*CO} - \Delta G_{*COOH}$, as both *COOH and *CO adsorption plays an important role in determining the reaction pathways. As shown in Figure 4A, volcano-shaped relationships are established for coordinately-unsaturated TM-CTFs and coordinately-saturated TM-TPPs[49] with Ni-CTF (η^{CO} = 0.34 V) and Co-TPP (η^{CO} = 0.78 V) located at the top of volcano, respectively. Overall, TM-CTFs with

coordinately-unsaturated TM are much better than the TM-TPPs with coordinately-saturated TM sites. Ni-CTF stands out as the best catalyst for CO_2RR among these catalysts. This prediction is supported by the previous experimental results that Co-CTF, Ni-CTF, and Cu-CTF have higher faraday efficiency (FE^{CO}) and current density (j) under the same conditions than the corresponding Co-TPP, Ni-TPP and Cu-TPP.[26] Furthermore, most of TM-CTFs have better CO_2RR catalytic activity than noble metals such as Ag[50] and Au[51], which are regarded as the state-of-the-art catalysts for CO_2RR. Thus, the TM-CTFs are a class of catalyst candidates with highly catalytic activity and expected to replace the noble metal catalysts.

Although a volcanic relationship has been established by using the adsorption energy as a descriptor, it is of more interest to identify an intrinsic descriptor that has a predictive power without further DFT calculations to guide the screening of the best catalysts from numerous material candidates. Recently, the *d*-band center[52], crystal field stabilization energy (CFSE)[45], e_g occupancy[53], t_{2g} occupancy[54] and *p*-band center[55-56] have been employed as descriptors to describe the catalytic activity of ORR, OER, HER on TM or TM-based catalysts. However, little work is done on coordinately-unsaturated TM-CTFs for the more complex CO_2RR. To establish a volcanic relationship with the overpotential (η^{CO}) for TM-CTFs, we have discovered a simple but inherent descriptor (Φ) defined by:

$$\Phi = \frac{N}{r_{TM} \times n}$$

where N, r_{TM}, and n are the number of *d* electrons, atomic radius, and periodic number of TMs (detailed in Supporting information). There is a positive correlation between the descriptor and the adsorption energy of intermediates or the bond strength of TM-intermediates, as shown in Figure S12A. Therefore, this descriptor, relating to the adsorption or bond strength of intermediates, represents the intrinsic characteristic of TM-CTFs, which has a certain physical meaning. Figure S12B is the volcano relationship between the descriptor and overpotential (η^{CO}) for all TM-CTFs, and the Ni-CTF (η^{CO} = 0.34 V) locates on the top of the volcano followed by Co-CTF (η^{CO} = 0.42 V) and Cu-CTF (η^{CO} = 0.51 V), which would show excellent catalytic activity in

the electroreduction of CO_2 to CO because their overpotentials are lower than that of noble Ag and Au catalysts. Accordingly, the catalysts with a descriptor (Φ) range from 0.80 to 1.30 could have high CO_2RR catalytic activity ($\eta^{CO} < 0.55$ V), which perform better than noble metals, Au ($\eta^{CO} = 0.70$ V) and Ag ($\eta^{CO} = 0.86$ V). In addition, the new descriptor also works well for coordinately-saturated TM-TPPs (Figure S12).

In addition to the prediction of the best catalysts, the catalytic mechanism can also be intuitively distinguished by using this descriptor for both coordinately-saturated and unsaturated COFs. As shown in Figure 4B, four regions are clearly differentiated to correspond to four reaction mechanisms: a) Regime 1 with $\Phi < 1.02$, in which CO_2RR toward CO proceeds via Path 1, on Ti, V, Cr-CTFs catalysts; b) Regime 2 with $1.02 < \Phi < 2.00$, where CO_2RR is favored to Path 2 on Mn, Fe, Co, Ni-CTFs; c) Regime 3 with $2.00 < \Phi < 2.32$, where Path 3 dominates CO_2RR on Cu-CTF; d) Regime 4 with $\Phi > 2.32$, where CO_2RR follows Path 4 on Zn-CTFs. Moreover, the CO_2RR catalytic mechanism on 4d or 5d TM-CTFs can also be predicted, as shown in Figure S13. Therefore, the descriptor (Φ) provides an effective tool for quickly predicting the CO_2RR catalytic activity and mechanisms of TM-CTFs.

The above predictions are consistent with the previous experimental results (Table S10). We have extracted current density (*j*) and the lowest Tafel plots from the literature.[26] As shown in Figure 4C, similar volcano-shaped relationships between the experimental results and the descriptor are established, in which the Ni-CTF exhibits the best catalytic performance, as predicted in this study. Thus, this novel descriptor can serve as reliable design principle to guide the synthesis of highly-performance catalysts.

We also explore the effect of the number of coordinates of TM in COFs on CO_2RR. As shown in Figure S14, four NiN_x based catalysts with different coordinate number (x = 2 to 5) anchored in graphene substrates are designed to calculate their CO_2RR catalytic behavior. The coordinately-saturated catalysts with high coordinate number (e.g. NiN_5 and NiN_4) have poor activity for CO_2 chemisorption and CO_2 activation, resulting a large overpotential (η^{CO} = 1.29 eV/NiN_5 or 1.15 eV/NiN_4) and poor CO_2RR catalytic performance. Those catalysts with coordinately-unsaturated TM

in its unit, namely NiN_3 and NiN_2, provide flexible modes in decreasing the adsorption energy of CO_2 and intermediates. Thus, coordinately unsaturated catalysts exhibit higher CO_2RR catalytic activity than the catalysts with coordinately-saturated TM unit, as shown in Figure 4d.

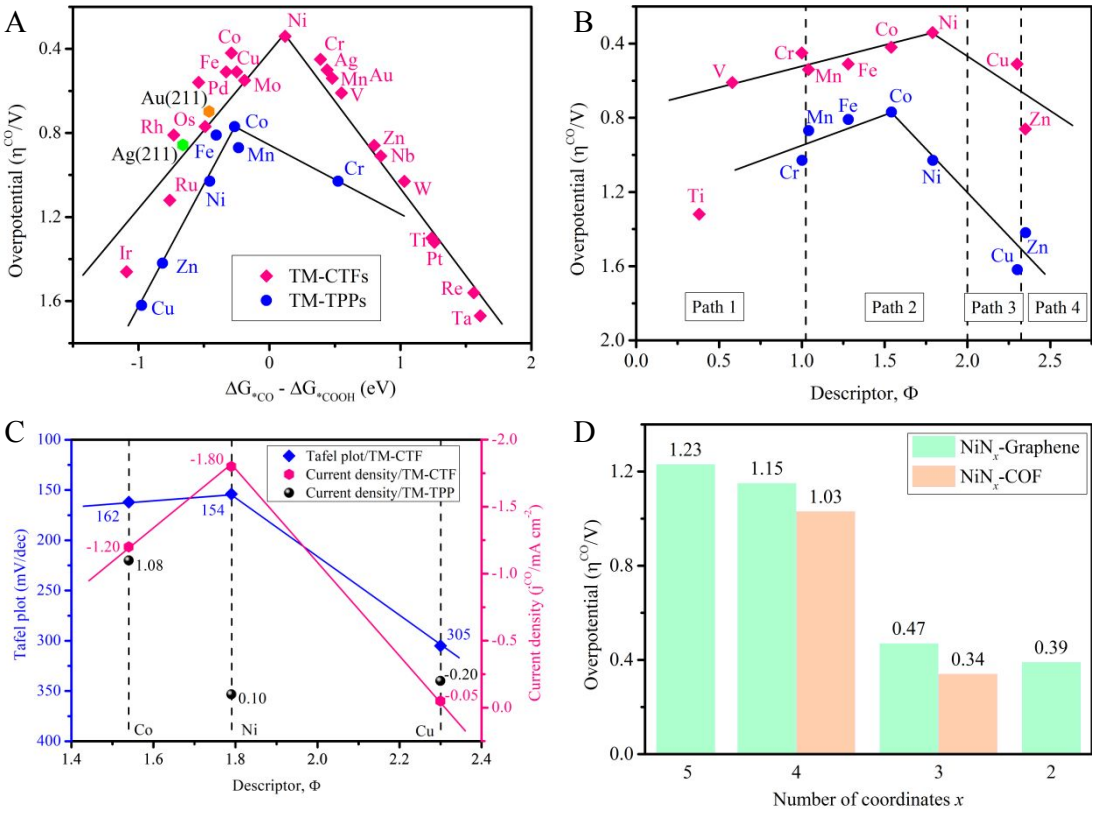

Figure 4. (A) Volcano-shape relationships between the overpotential (η^{CO}) and the adsorption energy of $\Delta G_{*CO} - \Delta G_{*COOH}$ for TM-CTFs and partial 3d TM-TPPs, the pink (round), black (square), orange (hexagon) and green (hexagon) represent TM-CTFs, TM-TPPs, noble Au and Ag, respectively. (B) Volcano-shape relationship between the overpotential (η^{CO}) and descriptor for 3d TM-CTFs. (C) The Tafel plot (mV/dec) and current density (j^{CO}/mA cm^{-2}) as a function of descriptor. [26] (D) The overpotential (η^{CO}) of NiN_x based catalysts with different coordinate number (x = 2 to 5), together with Ni-TPP and Ni-CTF.

2.4 Competing Reactions and Selectivity Predictions

The formic (HCOOH) or formate is a possible product that competes with CO in CO_2RR. Thus, we simulated the electrocatalytic CO_2RR to HCOOH under the same conditions. The CO_2RR towards HCOOH on TM-CTFs follows the following pathway: $CO_2 \rightarrow *CO_2 \rightarrow *OCHO \rightarrow *HCOOH \rightarrow HCOOH_{(l)}$. Notably, the process of producing HCOOH from *COOH can be excluded since according to the transition state (TS) calculation, there is a large energy barrier for the protonation of the inner C atom than that of the external O atom at the second hydronation reaction (Figure S17).

Thermodynamically, a catalyst with a high selectivity should have lower overpotential for CO than its competitors. Therefore, we plotted the overpotential of CO (η^{CO}) versus that of HCOOH (η^{HCOOH}) to determine whether CO or HCOOH is the dominant product in CO_2RR. As shown in Figure S18A, most of the TM-CTFs located at CO-dominated region ($\eta^{CO} < \eta^{HCOOH}$) except Ru-, Rh-, Ta-, Ir-, and Pt-CTFs that promote HCOOH. Figure S15 shows the free energy diagrams of these five catalysts for HCOOH. In fact, experiments have confirmed that the Rh- Ru-, Ir-, Pt-based catalysts are favored to produce HCOOH in electrocatalytic CO_2RR.[57-60] In particular, Rh-CTF (0.57 V), Ru-CTF (0.54 V), Ir-CTF (0.43 V), and Pt-CTF (0.49 V) catalysts have the activity comparable to Pt-based noble catalysts (0.17 V) and $CuSn_3$ catalysts (0.39 V) in electroreduction CO_2 to HCOOH. The volcano-shaped relationships can also be established by the adsorption energy difference of $\Delta G_{*HCOOH} - \Delta G_{*OCHO}$ or descriptor (Φ) versus the overpotential of HCOOH (η^{HCOOH}), as shown in Figure S16.

In addition, H_2 also competes with CO and HCOOH in CO_2RR since the thermodynamic potential of HER is very close to that of CO_2RR.[61] Similarly, the overpotential (η^{CO} *vs* η^{H2} or η^{HCOOH} *vs* η^{H2}) was also utilized to predict the preference of CO_2RR and HER on TM-CTFs. The overpotential of HER (η^{H2}) was calculated and listed in Table S7, together with CO_2RR (η^{CO}, η^{HCOOH}). As shown in Figure S18, Mn-, Fe-, Co-, Ni-, Ag- and Au-CTFs locate at CO-dominated region ($\eta^{CO} < \eta^{H2}$) and would have strong ability to suppress HER. On the other hand, Ir- and Pt-CTFs have lower overpotential for HCOOH than that for H_2 ($\eta^{HCOOH} < \eta^{H2}$), and may preferentially catalyze CO_2RR toward HCOOH. Thus, eight TM-CTFs are promising candidates with high activity and selectivity for CO_2RR to produce CO or HCOOH.

It is of importance to quantitatively predict the selectivity of the catalysts such that the efficiency of final products could be determined under different conditions. So far, there is no quantitative measure from computation approaches to determine the selectivity of the catalysts. Here, we introduce a simple parameter, the ratio of overpotentials of H_2 (η^{H2}) to CO (η^{CO}) as an index of selectivity since it represents relative compatibility between two competing chemical products (CO and H_2) at the same active sites under the same conditions. Figure 5A shows the ratio (η^{H2}/η^{CO}) as a function of the descriptor (Φ). We found that the descriptor also established a volcanic relationship of the selectivity with a flat summit in the regime of $1< \Phi < 2$, in which TM-CTFs and TM-TPPs are expected to exhibit high selectivity for CO_2RR to CO. Our prediction fit with the previous experimental data that the ratio of onset potential measured in experiments versus the descriptor also exhibits a similar volcanic relationship, as shown in Figure 5B.

The above predictions are also consistent with the previous experiments on Faraday efficiency (FE). It is well-known that the Faraday efficiency of CO is an important indicator to represent the overall conversion efficiency or selectivity of the catalytic systems in competition with HER. We have cited the Faraday efficiency of various M-N-C SACs and TM-CTFs from the literatures and made a plot of the reported FE versus the descriptor (Figure 5C). In spite of data scattering due to different measuring conditions, the results show a volcano-shaped plot, which is consistent with the predictions for the volcano in Figure 5A. Therefore, the ratio of overpotentials of H_2 (η^{H2}) to CO (η^{CO}) can be used as an effective index to predict the selectivity of the catalysts at different conditions.

The effect of the TM coordinates on the catalytic efficiency is also verified experimentally. As shown in Figure 5D, the Faraday efficiency of the catalysts increases with reducing the coordination number, i.e, the catalysts with coordinately-unsaturated have higher Faraday efficiency than the coordinately-saturated catalysts. These experimental results are consistent with our predictions shown in Figure 4D. This demonstrates the predictive power of the descriptor for not only catalytic activity but

also selectivity, guiding the rational design of highly active and selective TM-CTFs for CO_2 conversion.

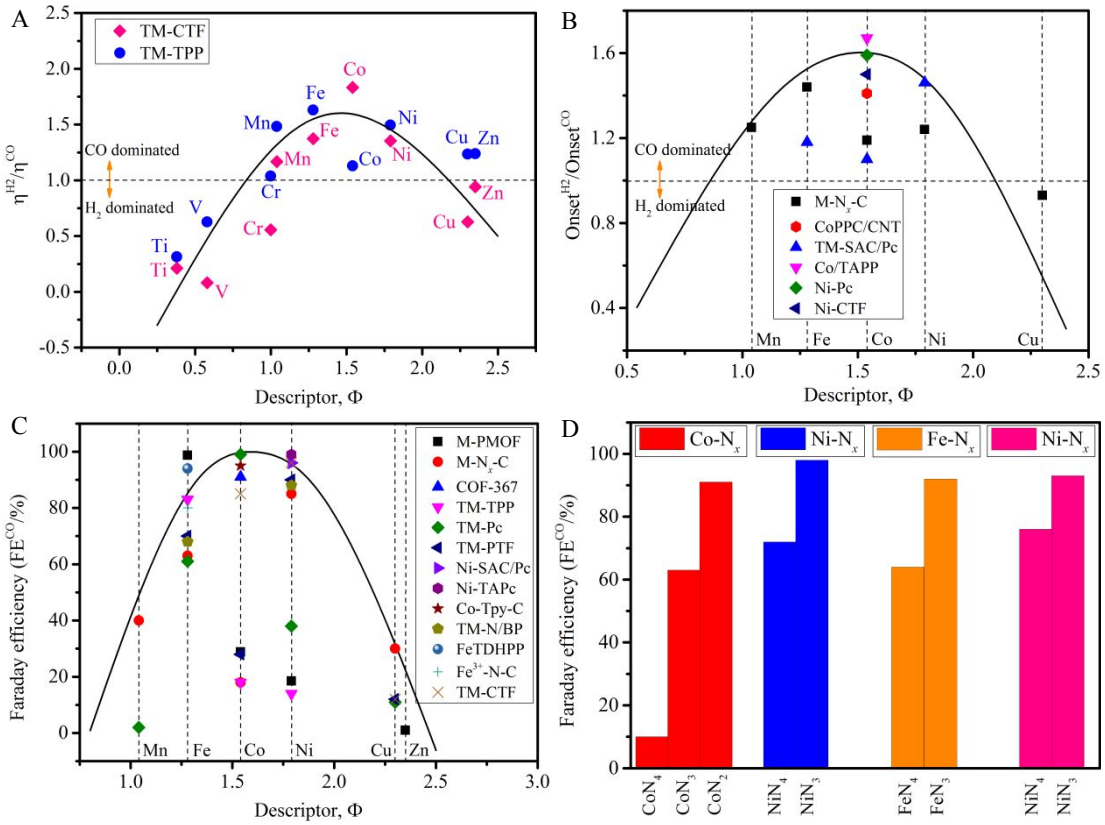

Figure 5. (A) The ratio between calculated overpotential of H_2 (η^{H2}) and CO (η^{CO}) as a function of the descriptor, predicted by the DFT calculations; (B) The ratio between experimental onset potential of H_2 (η^{H2}) and CO (η^{CO}) as a function of the descriptor, measured in the experiments[49, 62-65]; (C) The experimental results of Faraday efficiency (FE^{CO}) as a function of the descriptor [13, 49, 62-69]; (D) Faraday efficiency (FE^{CO}) of the FeN_x, CoN_x and NiN_x based catalysts with different coordination number[70-73].

It should be noted here that the current study focuses on CTF with single TM. It is possible to further enhance the catalytic activity by introducing dual or tri TM in CTF to form bimetallic or trimetallic catalysts (Figure S19). Thus, we further explored the CO_2RR catalytic activity on those TM-CTFs with single, double, triple TMs. As shown in Figure S20, the overpotential (η^{CO}) change range from -0.02 V to 0.04 V for Fe, Co,

Ni active sites. Thus, the influence of the second (Ni_2-CTF, Ni,Fe-CTF, Ni,Co-CTF) or third metal (Ni_3-CTF) is almost negligible. We also consider the effect of atomic size and select doping elements with relatively large atomic radius, including Mo (r = 1.90 Å) and Os (r = 1.85 Å) to replace Ni (r = 1.63 Å) in other two active sites. The overpotential of the three active sites in Ni, Mo, Os-CTF trimetallic catalysts increases by approximately 0.10 V compared with Ni-CTF. Therefore, the catalytic activity will be affected significantly by introducing one or more TMs with large atomic radius. Although the activity is not improved significantly with heterometal, the bi- or tri-metal sites could be designed to achieve cascade reactions in which different sites are specialized to catalyze different reactions, like a two-pot tandem reaction of CO_2RR on alloys.[74]

3 Conclusion

The CO_2RR catalytic behaviors on TM-CTFs have been systematically investigated by means of DFT to understand the catalytic mechanism and predict catalytic activity and selectivity. Volcano-shaped relationships have been established by using the intrinsic characteristics as effective descriptors, from which the best activity and selectivity of catalyst could be directly predicted. The corresponding catalytic mechanism of catalysts could also be easily distinguished from the volcanic map. Among the catalysts, Ni-CTF have the highest catalytic activity (η^{CO} = 0.34 V) in electroreduction CO_2 to CO, and most of the TM-CTFs with coordinately unsaturated TM active sites exhibit better CO_2RR catalytic activity than TM-TPPs with coordinately-saturated TM sites. Eight catalysts, namely Mn-CTF (η^{CO} = 0.54 V), Fe-CTF (η^{CO} = 0.51 V), Co-CTF (η^{CO} = 0.42 V), Ni-CTF (η^{CO} = 0.34 V), Ag-CTF (η^{CO} = 0.50 V), Au-CTF (η^{CO} = 0.54 V), Ir-CTF (η^{HCOOH} = 0.43 V) and Pt-CTF (η^{HCOOH} = 0.49 V), are expected to be promising candidates for CO_2RR, which have lower overpotential to inhibit the undesirable competitive reaction of HER. The predictions are supported by the previous experimental results from the literatures. This work provides a principle for guiding the rational design and screening of highly active and selective catalysts for CO_2RR.

Computation Methods

The Vienna Ab initio Simulation Package (VASP) code based on the density functional theory (DFT) was utilized to explore the catalytic behavior of CO_2RR on TM-CTFs.[75-76] The gradient corrected approximation of Perdew-Burke-Ernzerhof (GGA-PBE) functional was utilized to calculate the exchange-correlation energy, and the project-augmented wave generalized gradient approximation pseudopotentials (PAW-GGA) were adopted to describe the electron-ion interaction.[77-78] The Hubbard U (DFT+U) corrections was considered in the calculations and the values of the correction are listed in Table S1.[45] Wave functions were expanded using a plane-wave basis set with kinetic energy cutoff of 550 eV with a Gamma K-point grid of 3 × 3 × 1 for the Brillouin zone sampling for structural optimization or 5 × 5 × 1 for calculation of the density of state (DOS). The self-consistent field (SCF) were fully relaxed until the residual force convergence threshold of 0.01 eV/Å. A vacuum spacing of at least 20Å in z-direction perpendicular was employed to avert the artificial interactions between the periodically repeated images. Spin-polarization was considered in all calculations. The above parameters have been optimized until the energy change is negligible. The CO_2RR catalytic behavior on commercial noble electrocatalysts of Ag (2 1 1) and Au (2 1 1) were also simulated and the results are listed in Table S8. A p(4 × 4) unit cell was chose for both catalysts. Four layers were built in their slab configuration. The Crystal orbital Hamilton population (COHP) analysis was carried out using the Lobster program (Local Orbital Basis Suite Towards Electronic-Structure Reconstruction).[79-80] More details about computational methods for thermodynamic-related values are described in Supporting Information.

Acknowledgement

L.G., L.Z., X.H., and J.Z. thank the National Key Research and Development Program of China (2017YFA0206500), National Natural Science Foundation of China (51732002, 52073020), Distinguished Scientist Program at BUCT (buctylkxj02), the Fundamental Research Funds for the Central Universities（buctrc202008）and China

Scholarships Council (No.201806880044). ZX, and XW thank U.S. National Science Foundation (1561886 and 1662288) for the support of this research.

Author Contributions

Z.X. and L.G. conceived and designed the research. L.G., and D.Z. performed modelling and simulation, L.G. and Z.X. wrote the manuscript. All authors discussed the results and commented on the manuscript.

Declaration of Interests

The authors declare no competing interests.

References

[1]. Hansen, H. A.; Varley, J. B.; Peterson, A. A.; Nørskov, J. K. Understanding Trends in the Electrocatalytic Activity of Metals and Enzymes for CO_2 Reduction to CO. *J. Phys. Chem. Lett.* **2013**, *4*, 388–392.

[2]. Kuhl, K. P.; Cave, E. R.; Abram, D. N.; Jaramillo, T. F. New insights into the electrochemical reduction of carbon dioxide on metallic copper surfaces. *Energy Environ. Sci.* **2012**, *5*, 7050–7059.

[3]. Ma, M.; Djanashvili, K.; Smith, W. A. Controllable Hydrocarbon Formation from the Electrochemical Reduction of CO_2 over Cu Nanowire Arrays. *Angew. Chem.* **2016**, *128*, 6792–6796.

[4]. Hu, C.; Gong, L.; Xiao, Y.; Yuan, Y.; Bedford, N. M; Xia, Z.; Ma, L.; Wu, T.; Lin, Y.; Connell, J. W; Shahbazian-Yassar, R.; Lu, J.; Amine, K.; Dai, L. High-Performance, Long-Life, Rechargeable Li–CO_2 Batteries based on a 3D Holey Graphene Cathode Implanted with Single Iron Atoms. *Adv. Mater.* **2020**, *32*, 1907436.

[5]. Gong, L. L.; Feng, X. F.; Luo, F. Novel azo-Metal–Organic Framework Showing a 10-Connected bct Net, Breathing Behavior, and Unique Photoswitching Behavior toward CO_2. *Inorg. Chem.* **2015**, *54*, 11587–11589.

[6]. Bonin, J.; Maurin, A.; Robert, M. Molecular catalysis of the electrochemical and

photochemical reduction of CO_2 with Fe and Co metal based complexes. Recent advances. *Coord. Chem. Rev.* **2017**, *334*, 184–198

[7]. Choi, J.; Wagner, P.; Jalili, R.; Kim, J.; MacFarlane, D. R.; Wallace, G. G.; Officer, D. L. A porphyrin/graphene framework: a highly efficient and robust electrocatalyst for carbon dioxide reduction. *Adv. Energy Mater.* **2018**, *8*, 1801280.

[8]. Vasileff, A.; Zheng, Y.; Qiao, S. Z. Carbon Solving Carbon's Problems: Recent Progress of Nanostructured Carbon-Based Catalysts for the Electrochemical Reduction of CO_2. *Adv. Energy Mater.* **2017**, *7*, 1700759.

[9]. Lin, S.; Diercks, C. S.; Zhang, Y.-B.; Kornienko, N.; Nichols, E. M.; Zhao, Y.; Paris, A. R.; Kim, D.; Yang, P.; Yaghi, O. M.; Chang, C. J. Covalent organic frameworks comprising cobalt porphyrins for catalytic CO_2 reduction in water. *Science* **2015**, *349*, 1208–1213.

[10]. Jiang, K.; Wang, H. Electrocatalysis over graphene-defect-coordinated transition-metal single-atom catalysts. *Chem* **2018**, *4*, 194–195.

[11]. Huan, T. N.; Ranjbar, N.; Rousse, G.; Sougrati, M.; Zitolo, A.; Mougel, V.; Jaouen, F.; Fontecave, M. Electrochemical Reduction of CO_2 Catalyzed by Fe-NC Materials: A Structure–Selectivity Study. *ACS Catal.* **2017**, *7*, 1520−1525.

[12]. Hu, X.-M.; Rønne, M. H.; Pedersen, S. U.; Skrydstrup, T.; Daasbjerg, K. Enhanced Catalytic Activity of Cobalt Porphyrin in CO_2 Electroreduction upon Immobilization on Carbon Materials. *Angew. Chem. Int. Ed.* **2017**, *56*, 6468–6472.

[13]. Liu, S.; Yang, H. B.; Hung, S.-F.; Ding, J.; Cai, W.; Liu, L.; Gao, J.; Li, X.; Ren, X.; Kuang, Z.; Huang, Y.; Zhang, T.; Liu, B. Elucidating the Electrocatalytic CO_2 Reduction Reaction over a Model Single-Atom Nickel Catalyst. *Angew. Chem. Int. Ed.* **2020**, *59*, 798–803.

[14]. Wang, Y.; Han, P.; Lv, X.; Zhang, L.; Zheng, G. Defect and Interface Engineering for Aqueous Electrocatalytic CO_2 Reduction. *Joule* **2018**, *2*, 2551–2582.

[15]. Zheng, W.; Yang, J.; Chen, H.; Hou, Y.; Wang, Q.; Gu, M.; He, F.; Xia, Y.; Xia, Z.; Li, Z.; Yang, B.; Lei, L.; Yuan, C.; He, Q.; Qiu, M.; Feng, X. Atomically Defined Undercoordinated Active Sites for Highly Efficient CO_2 Electroreduction.

Adv. Funct. Mater. **2020**, *30*, 1907658.

[16]. Rong, X.; Wang, H.-J.; Lu, X.-L.; Si, R.; Lu, T.-B. Controlled Synthesis of a Vacancy-Defect Single-Atom Catalyst for Boosting CO_2 Electroreduction. *Angew. Chem. Int. Ed.* **2020**, *59*, 1961–1965.

[17]. Zhao, Z.; Chen, Z.; Zhang, X.; Lu, G. Generalized Surface Coordination Number as an Activity Descriptor for CO_2 Reduction on Cu Surfaces. *J. Phys. Chem. C* **2016**, *120*, 28125–28130.

[18]. Li, H.; Li, Y.; Koper, M. T. M.; Calle-Vallejo, F. Bond-making and breaking between carbon, nitrogen, and oxygen in electrocatalysis. *J. Am. Chem. Soc.* **2014**, *136*, 15694–15701.

[19]. Yan, C.; Li, H.; Ye, Y.; Wu, H.; Cai, F.; Si, R.; Xiao, J.; Miao, S.; Xie, S.; Yang, F.; Li, Y.; Wang, G.; Bao, X. Coordinatively unsaturated nickel–nitrogen sites towards selective and high-rate CO_2 electroreduction. *Energy Environ. Sci.* **2018**, *11*, 1204–1210.

[20]. Iwase, K.; Nakanishi, S.; Miyayama, M.; Kamiya K. Rational Molecular Design of Electrocatalysts Based on Single-Atom Modified Covalent Organic Frameworks for Efficient Oxygen Reduction Reaction. *ACS Appl. Energy Mater.* **2020**, *3*, 1644–1652.

[21]. Wang, Y.-R.; Huang, Q.; He, C.-T.; Chen, Y.; Liu, J.; Shen, F.-C.; Lan, Y.-Q. Oriented electron transmission in polyoxometalate-metalloporphyrin organic framework for highly selective electroreduction of CO_2. *Nat. Commun.* **2018**, *9*, 4466.

[22]. Diercks, C. S.; Lin, S.; Kornienko, N.; Kapustin, E. A.; Nichols, E. M.; Zhu, C.; Zhao, Y.; Chang, C. J.; Yaghi, O. M. Reticular electronic tuning of porphyrin active sites in covalent organic frameworks for electrocatalytic carbon dioxide reduction. *J. Am. Chem. Soc.* **2018**, *140*, 1116–1122.

[23]. Liu, Y.; Yan, X.; Li, T.; Zhang, W.-D.; Fu, Q.-T.; Lu, H.-S.; Wang, X.; Gu, Z.-G. Three-dimensional porphyrin-based covalent organic frameworks with tetrahedral building blocks for single-site catalysis. *New J. Chem*. **2019**, *43*, 16907–16914.

[24]. Rybicka-Jasińska, K.; Shan, We.; Zawada, K.; Kadish, K. M.; Gryko, D. Porphyrins as Photoredox Catalysts: Experimental and Theoretical Studies. *J. Am. Chem. Soc.* **2016**, *138*, 15451–15458.

[25]. Zion, N.; Cullen, D. A.; Zelenay, P.; Elbaz, L. Heat-Treated Aerogel as a Catalyst for the Oxygen Reduction Reaction. *Angew. Chem. Int. Ed.* **2020**, *59*, 2483–2489.

[26]. Su, P.; Iwase, K.; Harada, T.; Kamiya, K.; Nakanishi, S. Covalent triazine framework modified with coordinatively-unsaturated Co or Ni atoms for CO_2 electrochemical reduction. *Chem. Sci.* **2018**, *9*, 3941–3947.

[27]. Puthiaraj, P.; Lee, Y.-R.; Zhang, S.; Ahn, W.-S. Triazine-based covalent organic polymers: design, synthesis and applications in heterogeneous catalysis. *J. Mater. Chem. A* **2016**, *4*, 16288–16311.

[28]. Wang, K.; Yang, L.-M.; Wang, X.; Guo, L.; Cheng, G.; Zhang, C.; Jin, S.; Tan, B.; Cooper, A. Covalent triazine frameworks via a low-temperature polycondensation approach. *Angew. Chem. Int. Ed.* **2017**, *56*, 14149–14153.

[29]. Yoshioka, T.; Iwase, K.; Nakanishi, S.; Hashimoto, K.; Kamiya, K. Electrocatalytic reduction of nitrate to nitrous oxide by a copper-modified covalent triazine framework. *J. Phys. Chem. C* **2016**, *120*, 15729−15734.

[30]. Iwase, K.; Yoshioka, T.; Nakanishi, S.; Hashimoto, K.; Kamiya, K. Copper-Modified Covalent Triazine Frameworks as Non-Noble-Metal Electrocatalysts for Oxygen Reduction. *Angew. Chem. Int. Ed.* **2015**, *54*, 11068–11072.

[31]. Kamai, R.; Kamiya, K.; Hashimoto, K.; Nakanishi, S. Oxygen-Tolerant Electrodes with Platinum-Loaded Covalent Triazine Frameworks for the Hydrogen Oxidation Reaction. *Angew. Chem. Int. Ed.* **2016**, *55*, 13378–13382.

[32]. Kamiya, K.; Kamai, R.; Hashimoto, K.; Nakanishi, S. Platinum-modified covalent triazine frameworks hybridized with carbon nanoparticles as methanol-tolerant oxygen reduction electrocatalysts. *Nat. Commun.* **2014**, *5*, 5040.

[33]. Iwase, K.; Kamiya, K.; Miyayama, M.; Hashimoto, K.; Nakanishi, S. Sulfur-Linked Covalent Triazine Frameworks Doped with Coordinatively

Unsaturated Cu (I) as Electrocatalysts for Oxygen Reduction. *ChemElectroChem* **2018**, *5*, 805–810.

[34]. Guo, X.; Gu, J.; Lin, S.; Zhang, S.; Chen, Z.; Huang, S. Tackling the Activity and Selectivity Challenges of Electrocatalysts toward the Nitrogen Reduction Reaction via Atomically Dispersed Biatom Catalysts. *J. Am. Chem. Soc.* **2020**, *142*, 5709–5721.

[35]. Guo, X.; Lin, S.; Gu, J.; Zhang, S.; Chen, Z.; Huang, S. Simultaneously Achieving High Activity and Selectivity toward Two-Electron O_2 Electroreduction: The Power of Single-Atom Catalysts. *ACS Catal.* **2019**, *9*, 11042–11054.

[36]. Yamaguchi, S.; Kamiya, K.; Hashimoto, K.; Nakanishi, S. Ru atom-modified covalent triazine framework as a robust electrocatalyst for selective alcohol oxidation in aqueous electrolytes. *Chem. Commun.* **2017**, *53*, 10437–10440.

[37]. Palkovits, R.; Antonietti, M.; Kuhn, P.; Thomas, A.; Schüth, F. Solid catalysts for the selective low-temperature oxidation of methane to methanol. *Angew. Chem. Int. Ed.* **2009**, *48*, 6909 –6912.

[38]. Kamai, R.; Nakanishi, S.; Hashimoto, K.; Kamiya, K. Selective electrochemical reduction of nitrogen oxides by covalent triazine frameworks modified with single Pt atoms. *J. Electroanal. Chem.* **2017**, *800*, 54–59.

[39]. Bavykina, A. V.; Olivos-Suarez, A. I.; Osadchii, D.; Valecha, R.; Franz, R.; Makkee, M.; Kapteijn, F.; Gascon, J. Facile method for the preparation of covalent triazine framework coated monoliths as catalyst support: Applications in c1 catalysis. *ACS Appl. Mater. Interfaces* **2017**, *9*, 26060−26065.

[40]. Kamiya, K.; Tatebe, T.; Yamamura, S.; Iwase, K.; Harada, T.; Nakanishi, S. Selective reduction of nitrate by a local cell catalyst composed of metal-doped covalent triazine frameworks. *ACS Catal.* **2018**, *8*, 2693−2698.

[41]. Park, K.; Gunasekar, G. H.; Prakash, N.; Jung, K.-D.; Yoon, S. A highly efficient heterogenized iridium complex for the catalytic hydrogenation of carbon dioxide to formate. *ChemSusChem* **2015**, *8*, 3410–3413.

[42]. Li, J.; Liu, P.; Tang, Y.; Huang, H.; Cui, H.; Mei, D.; Zhong, C. Single-Atom

Pt–N_3 Sites on the Stable Covalent Triazine Framework Nanosheets for Photocatalytic N_2 Fixation. *ACS Catal.* **2020**, 10, 2431−2442.

[43]. Lu, C.; Yang, J.; Wei, S.; Bi, S.; Xia, Y.; Chen, M.; Hou, Y.; Qiu, M.; Yuan, C.; Su, Y.; Zhang, F.; Liang, H.; Zhuang, X. Atomic Ni Anchored Covalent Triazine Framework as High Efficient Electrocatalyst for Carbon Dioxide Conversion. *Adv. Funct. Mater.* **2019**, *29*, 1806884.

[44]. Buyukcakir, O.; Je, S. H.; Talapaneni, S. N.; Kim, D.; Coskun, A. Charged Covalent Triazine Frameworks for CO_2 Capture and Conversion. *ACS Appl. Mater. Interfaces* **2017**, *9*, 7209–7216.

[45]. Lin, C.-Y.; Zhang, L.; Zhao, Z.; Xia, Z. Design principles for covalent organic frameworks as efficient electrocatalysts in clean energy conversion and green oxidizer production. *Adv. Mater.* **2017**, *29*, 1606635.

[46]. Duan, Z.; Wang, G. Comparison of reaction energetics for oxygen reduction reactions on Pt (100), Pt (111), Pt/Ni (100), and Pt/Ni (111) surfaces: a first-principles study. *J. Phys. Chem. C* **2013**, *117*, 6284–6292.

[47]. Zhang, L.; Niu, J.; Li, M.; Xia, Z. Catalytic mechanisms of sulfur-doped graphene as efficient oxygen reduction reaction catalysts for fuel cells. *J. Phys. Chem. C* **2014**, *118*, 3545−3553.

[48]. Zhang, L.; Lin, C.-Y.; Zhang, D.; Gong, L.; Zhu, Y.; Zhao, Z.; Xu, Q.; Li, H.; Xia, Z. Guiding Principles for Designing Highly Efficient Metal-Free Carbon Catalysts. *Adv. Mater.* **2018**, *31*, 1805252.

[49]. Gong, L.; Zhang, D.; Lin, C.-Y.; Zhu, Y.; Shen, Y.; Zhang, J.; Han, X.; Zhang, L.; Xia, Z. Catalytic Mechanisms and Design Principles for Single-Atom Catalysts in Highly Efficient CO_2 Conversion. *Adv. Energy Mater.* **2019**, *9*, 1902625.

[50]. Singh, M. R.; Goodpaster, J. D.; Weber, A. Z.; Head-Gordon, M.; Bell, A. T. Mechanistic insights into electrochemical reduction of CO_2 over Ag using density functional theory and transport models. *Proc. Natl. Acad. Sci. U.S.A.* **2017**, *114*, E8812−E8821.

[51]. Zhu, W.; Michalsky, R.; Metin, Ö.; Lv, H.; Guo, S.; Wright, C. J.; Sun, X.; Peterson, A. A.; Sun, S.; Monodisperse Au Nanoparticles for Selective

Electrocatalytic Reduction of CO_2 to CO. *J. Am. Chem. Soc.* **2013**, *135*, 16833−16836.

[52]. Hammer, B.; Norskov, J. K. Theoretical surface science and catalysis—calculations and concepts. *Adv. Catal.* **2000**, *45*, 71−129.

[53]. Suntivich, J.; Gasteiger, H. A.; Yabuuchi, N.; Nakanishi, H.; Goodenough, J. B.; Shao-Horn, Y. Design principles for oxygen-reduction activity on perovskite oxide catalysts for fuel cells and metal–air batteries. *Nat. Chem.* **2011**, 3, 546−550.

[54]. Toyoda, K.; Hinogami, R.; Miyata, N.; Aizawa, M. Calculated descriptors of catalytic activity for water electrolysis anode: application to delafossite oxides. *J. Phys. Chem. C* **2015**, *119*, 6495−6501.

[55]. Grimaud, A.; May, K. J.; Carlton, C. E.; Lee, Y.-L.; Risch, M.; Hong, W. T.; Zhou, J.; Shao-Horn, Y. Double perovskites as a family of highly active catalysts for oxygen evolution in alkaline solution. *Nat. Commun.* **2013**, 4, 2439.

[56]. Sinthika, S.; Waghmare, U. V.; Thapa, R. Structural and electronic descriptors of catalytic activity of graphene-based materials: first-principles theoretical analysis. *Small* **2017**, 14, 1703609.

[57]. Birdja, Y. Y.; Shen, J.; Koper, M. T. M. Influence of the metal center of metalloprotoporphyrins on the electrocatalytic CO_2 reduction to formic acid. *Catal. Today* **2017**, *288*, 37−47.

[58]. Spataru, N.; Tokuhiro, K.; Terashima, C.; Rao, T. N.; Fujishima, A. Electrochemical reduction of carbon dioxide at ruthenium dioxide deposited on boron-doped diamond. *J. Appl. Electrochem.* **2003**, *33*, 1205–1210.

[59]. Kang, P.; Cheng, C.; Chen, Z.; Schauer, C. K.; Meyer, T. J.; Brookhart, M. Selective Electrocatalytic Reduction of CO_2 to Formate by Water-Stable Iridium Dihydride Pincer Complexes. *J. Am. Chem. Soc.* **2012**, *134*, 5500–5503.

[60]. Kortlever, R.; Peters, I.; Koper, S.; Koper, M. T. M. Electrochemical CO_2 Reduction to Formic Acid at Low Overpotential and with High Faradaic Efficiency on Carbon-Supported Bimetallic Pd–Pt Nanoparticles. *ACS Catal.* **2015**, *5*, 3916–3923.

[61]. Zhang, W.; Hu, Y.; Ma, L.; Zhu, G.; Wang, Y.; Xue, X.; Chen, R.; Yang, S.;

Jin, Z. Progress and Perspective of Electrocatalytic CO_2 Reduction for Renewable Carbonaceous Fuels and Chemicals. *Adv. Sci.* **2018**, *5*, 1700275.

[62]. Lu, X.-L.; Rong, X.; Zhang, C.; Lu, T.-B. Carbon-based single-atom catalysts for CO_2 electroreduction: progress and optimization strategies. *J. Mater. Chem. A* **2020**, *8*, 10695–10708.

[63]. Wang, Q.; Lei, Y.; Wang, D.; Li, Y. Defect engineering in earth-abundant electrocatalysts for CO_2 and N_2 reduction. *Energy Environ. Sci.* **2019**, *12*, 1730–1750.

[64]. Qin, R.; Liu, K.; Wu, Q.; Zheng N.; Surface Coordination Chemistry of Atomically Dispersed Metal Catalysts. 10.1021/acs.chemrev.0c00094.

[65]. Zhao, C.; Wang, Y.; Li, Z.; Chen, We.; Xu, Q.; He, D.; Xi, D.; Zhang, Q.; Yuan, T.; Qu, Y.; Yang, J.; Zhou, F.; Yang, Z.; Wang, X.; Wang, J.; Luo, J.; Li, Y.; Duan, H.; Li, Y. Solid-diffusion synthesis of single-atom catalysts directly from bulk metal for efficient CO_2 reduction. *Joule*, **2019**, *3*, 584–594.

[66]. Su, P.; Iwase, K.; Nakanishi, S.; Hashimoto, K.; Kamiya, K. Nickel-nitrogen-modified graphene: an efficient electrocatalyst for the reduction of carbon dioxide to carbon monoxide. *Small* **2016**, *12*, 6083–6089.

[67]. Wang, L.; Zhang, J.; Zheng, L.; Yang, J.; Li, Y.; Wan, X.; Liu, X.; Zhang, X.; Yua, R.; Shui, J. Carbon Black Supported FM-NC (FM= Fe, Co, Ni) Single-Atom Catalysts Synthesized by Self-Catalysis of Oxygen Coordinated Ferrous Metal Atoms. *J. Mater. Chem. A* **2020**, *8*, 13166–13172.

[68]. Hou, Y.; Huang, Y.-B.; Liang, Y.-L.; Chai, G.-L.; Yi, J.-D.; Zhang, T.; Zang, K.-T.; Luo, J.; Xu, R.; Lin, H.; Zhang, S.-Y.; Wang, H.-M.; Cao, R. Unraveling the Reactivity and Selectivity of Atomically Isolated Metal–Nitrogen Sites Anchored on Porphyrinic Triazine Frameworks for Electroreduction of CO_2. *CCS Chemistry* **2019**, *1*, 384–395.

[69]. Wang, Y.; Jiang, Z.; Zhang, X.; Niu, Z.; Zhou, Q.; Wang, X.; Li, H.; Lin, Z.; Zheng, H.; Liang, Y. Metal Phthalocyanine-Derived Single-Atom Catalysts for Selective CO_2 Electroreduction under High Current Densities. *ACS Appl. Mater. Interfaces* **2020**, *12*, 33795–33802.

[70]. Sun, J.-F.; Wu, J.-T.; Xu, Q.-Q.; Zhou D.; Yin J.-Z. CO_2 electrochemical reduction using single-atom catalysts. Preparation, characterization and anchoring strategies: a review. *Environ. Chem. Lett.* **2020**, *18*, 1593–1623.

[71]. Wang, X.; Chen, Z.; Zhao, X.; Yao, T.; Chen, W.; You, R.; Zhao, C.; Wu, G.; Wang, J.; Huang, W.; Yang, J.; Hong, X.; Wei, S.; Wu, Y.; Li, Y. Regulation of Coordination Number over Single Co Sites: Triggering the Efficient Electroreduction of CO_2. *Angew. Chem. Int. Ed.* **2018**, *57*, 1944–1948.

[72]. Wang, T.; Sang, X.; Zheng, W.; Yang, B.; Yao, S.; Lei, C.; Li, Z.; He, Q.; Lu, J.; Lei, L.; Dai, L.; Hou, Y. Gas Diffusion Strategy for Inserting Atomic Iron Sites into Graphitized Carbon Supports for Unusually High-Efficient CO_2 Electroreduction and High-Performance Zn–CO_2 Batteries. *Adv. Mater.* **2020**, *32*, 2002430.

[73]. Daiyan, R.; Zhu, X.; Tong, Z.; Gong, L.; Razmjou, A.; Liu, R.-S.; Xia, Z.; Lu, X.; Dai, L.; Amal, R. Transforming active sites in nickel–nitrogen–carbon catalysts for efficient electrochemical CO_2 reduction to CO. *Nano Energy* **2020**, *78*, 105213.

[74]. Cheng, M.-J.; Clark, E. L.; Pham, H. H.; Bell, A. T.; Head-Gordon, M. Quantum Mechanical Screening of Single-Atom Bimetallic Alloys for the Selective Reduction of CO_2 to C_1 Hydrocarbons. *ACS Catal.* **2016**, *6*, 7769–7777.

[75]. Hirunsit, P. Electroreduction of carbon dioxide to methane on copper, copper–silver, and copper–gold catalysts: a DFT study. *J. Phys. Chem. C* **2013**, *117*, 8262–8268.

[76]. Grabow, L. C.; Mavrikakis, M. Mechanism of Methanol Synthesis on Cu through CO_2 and CO Hydrogenation. *ACS Catal.* **2011**, *1*, 365-384.

[77]. Solovyev, I. V.; Dederichs, P. H.; Anisimov, V. I. Corrected atomic limit in the local-density approximation and the electronic structure of d impurities in Rb. *Phys. Rev. B* **1994**, *50*, 16861–16871.

[78]. Perdew, J. P.; Burke, K.; Ernzerhof, M. Generalized Gradient Approximation Made Simple. *Phys. Rev. Lett.* 1997, 77, 3865–3868.

[79]. Deringer, V. L.; Tchougréeff, A. L.; Dronskowski, R. Crystal orbital Hamilton population (COHP) analysis as projected from plane-wave basis sets. *J. Phys.*

Chem. A **2011**, *115*, 5461–5466.

[80]. Maintz, S.; Deringer, V. L.; Tchougréeff, A. L.; Dronskowski, R. LOBSTER: A tool to extract chemical bonding from plane-wave based DFT. *J. Comput. Chem.* **2016**, *37*, 1030–1035.